Multiscale approach to model steady meniscus evaporation in a wetting fluid

Kishan Bellur [1,*] Ezequiel F. Médici,[1] Chang Kyoung Choi,[1]
James C. Hermanson,[2] and Jeffrey S. Allen[1]
[1]*Michigan Technological University, Houghton, Michigan, USA*
[2]*University of Washington, Seattle, Washington, USA*

Evaporation along a curved liquid vapor interface, such as that of a wetting meniscus, is a classic multiscale problem of vital significance to many fields of science and engineering. However, a complete description of the local evaporative flux over all length scales, especially without arbitrary tuning of boundary conditions, is lacking. A multiscale method to model evaporation from steady meniscus is described such that a need for tuning of boundary conditions and additional assumptions are alleviated. A meniscus submodel is used to compute evaporation flux in the bulk meniscus while a transition film submodel is used to account for enhanced evaporation near the contact line. A unique coupling between the meniscus and transition film submodels ensures smooth continuity of both film and mass flux profiles along the meniscus. The local mass flux is then integrated over the interfacial area to investigate the contribution from the different regions on the surface. The model is evaluated with data from cryoneutron phase-change tests conducted previously at National Institute for Standards and Technology (NIST) [K. Bellur *et al.*, Cryogenics **74**, 131 (2016)]. It is found that the peak mass flux in the transition region is two orders of magnitude greater than the flux at the apex. Despite the enhanced evaporation in the thin film region, it was found that 78–95% of the evaporation occurs in the bulk meniscus due to the large area. The bulk meniscus contribution increases with increase in vapor pressure and Bond number but decreases with an increase in thermal conductivity of the substrate. Using a nonuniform temperature boundary suggests that there is a possibility that the adsorbed film may have a nonzero mass flux.

I. INTRODUCTION

The ability to model and predict evaporation from curved liquid vapor interfaces such as that of a meniscus is vital in many fields, including but not limited to atmospheric science [1,2], aerosol transport [3,4], and micro- and nanoscale thermal transport in MEMS applications [5–7] and for designing large cryogenic depots critical to long-term space missions [8]. The kinetic theory of phase change is the current tool of choice to develop models where limiting factor is not the diffusive transport in the vapor phase but rather the interfacial kinetics. There are two cases where the diffusive model breaks down: (1) For a pure, single component liquid-vapor mixture, the vapor density is generally uniform except in a nanoscale region close to the interface. (2) As the interfacial area decreases with respect to the contact line length, the rate of evaporation is no longer proportional to the area as is implied by diffusive models [9]. The mass flux predicted from most diffusive models reaches a singularity at the three-phase contact point and an asymptotic treatment is necessary. It has been shown that kinetic effects regularize the mass flux singularity at the contact line [10].

---

*ksbellur@mtu.edu
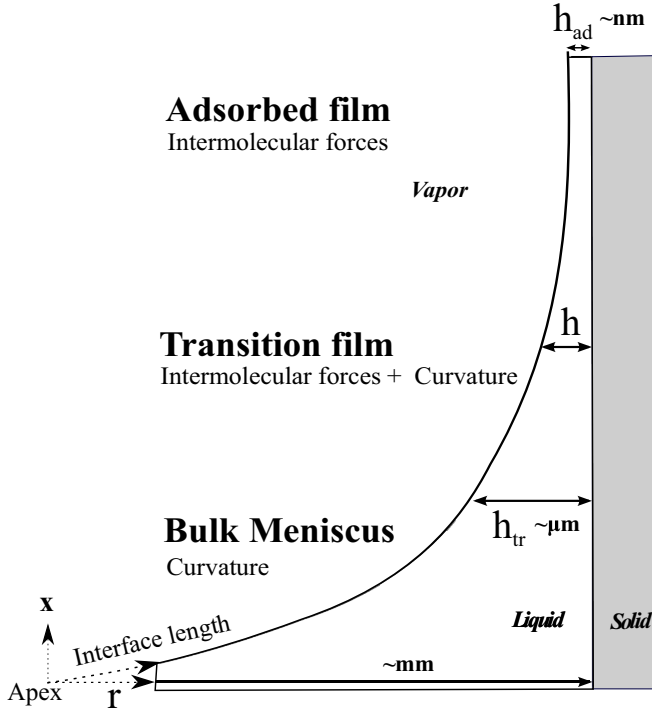
FIG. 1. Regions of an evaporating wetting meniscus. h_{tr} is an arbitrary film thickness used to distinguish the start of the transition region from the bulk meniscus. h_{ad} is the adsorbed film thickness, commonly assumed to be a uniform constant.

The most widely used kinetic approach to model phase change today was initially developed by Schrage [11] and the original formulation reduces to [12]:

$$\dot{m}'' = \frac{2\alpha}{2 - \alpha} \sqrt{\frac{m}{2\pi k_b}} \left(\frac{P_{li}}{\sqrt{T_i}} - \frac{P_{vi}}{\sqrt{T_v}} \right), \tag{1}$$

where $\dot{m}''$ is the mass flux, m is the mass of the molecule, k_b is the Boltzmann's constant, P_{li} is the liquid pressure at the interface, P_{vi} is the vapor pressure at the interface, T_i is the temperature of the liquid at the interface, T_v is the vapor temperature, and α is the accommodation coefficient defined as the ratio of molecules that undergo phase change. The magnitude of the coefficient must be between 0 and 1. The coefficients are determined empirically [13]. Despite decades of work on kinetic theory of phase change, measurements of the accommodation coefficient are inconsistent [3,14,15]. Even for a common fluid such as water, the reported values of coefficients vary by almost three orders of magnitude depending on the researcher or experimental method used [15]. Attempts to investigate and explain the discrepancy of measured values for these coefficients have not completely resolved this inconsistency [14–17].

Equation (1) was originally developed for a flat liquid-vapor interface such that there is no influence from a solid-liquid or solid-vapor interface. As the length scale is reduced, the distance between the liquid-vapor interface and the solid-liquid interface decreases and additional stresses are imposed on the liquid film that alter its shape and local interfacial thermodynamics.

Figure 1 delineates regions of interest along a wetting evaporating meniscus based on the dominant component of normal stress that affects the thermofluid dynamics and their approximate length scales. This delineation was first introduced by Wayner *et al.* [18]. The normal stress in

the bulk liquid is governed by capillary forces or interface curvature. The normal stress in the adsorbed film region is most affected by intermolecular forces and is usually a nanoscale film. The transition region bridges the bulk meniscus with the adsorbed film and experiences a mix of both intermolecular forces and curvature. Anisotropy of the stresses in thin liquid films is attributed to disjoining pressure, which is a net pressure reduction in thin films due to intermolecular forces [18]. Curvature of the liquid-vapor interface gives rise to a capillary pressure jump. Hence, there is a variation in the local thermodynamic states along the meniscus that result in a nonuniform evaporation flux over the interface [19].

Wayner *et al.* [18,20] adapted the planar kinetic model for phase change [Eq. (1)] for a curved interface. They used the Gibbs-Duhem equations for the bulk liquid and vapor phases coupled with surface tension to develop a fugacity expression for the local interfacial thermodynamics. The expression was then integrated over a region where small changes in fugacity can be assumed to be equal to the corresponding change in vapor pressure. If the vapor density is neglected in comparison to the liquid density and thermal equilibrium is assumed over the interface, then evaporation flux along a curved interface could be expressed by Eq. (2) [18,20],

$$\dot{m}'' = \frac{2\alpha}{2-\alpha}\left(\frac{M}{2\pi RT_i}\right)^{1/2}\left[\frac{p_v M h_{\mathrm{fg}}}{RT_v T_i}(T_i - T_v) - \frac{v_l p_v}{RT_i}(\Pi + \sigma\kappa)\right], \qquad (2)$$

where Π is disjoining pressure, σ is surface tension, h_{fg} is the enthalpy of vaporization, R is the universal gas constant, κ is the surface curvature, p_v is vapor pressure, M is molar mass, and v_l is molar volume. The first term denotes the thermal contribution and second term is the mechanical contribution to phase change.

Resistance to thermal transport between the solid-liquid interface and the liquid-vapor interface increases with liquid-film thickness. Hence, interfacial temperatures can vary significantly over the liquid-vapor interface even for a constant wall temperature. For nonpolar wetting liquids, the local evaporation flux in the transition region has been reported to be 3–9 times greater than that in the bulk meniscus [18,19,21–27]. This is due to the interplay of thermal transport in the thin film and the dominating normal stress component at the interface.

To investigate the enhanced evaporation in the thin transition-film region a large number of prior publications have used a one-dimensional (1D) lubrication approximation coupled with thermal transport in the thin film along with a kinetic model for the interface. Generally, the governing equations of mass, momentum, and energy are coupled using the augmented Young-Laplace equation. All quantities are expressed in terms of the film thickness in the form of an evolution equation. The coupled system could be solved to determine both the film and the mass flux profiles. The boundary conditions applied and solution methodologies have varied widely in literature. A few important studies are summarized below and tabulated in Table I. For a more exhaustive review of thin-film modeling, the reader is directed elsewhere [28,29].

Potash and Wayner [21] demonstrated that the change in disjoining and capillary pressure was sufficient for fluid flow into the thin film and required to sustain thin-film evaporation. They also showed the existence of a peak evaporative flux in the transition region. DasGupta *et al.* [30] developed a nonlinear system of equations based on the lubrication approximation, thermal transport, and interfacial transport. A Taylor-series expansion was used to adjust the boundary conditions. Several nondimensional parameters were adjusted to obtain a solution that matches the experimentally measured film profile. Film thickness at the adsorbed film was known *in situ*, eliminating the need for approximations. The adsorbed film was assumed to be nonevaporating. A Cartesian system with a single radii of curvature was considered and the wall temperature was assumed to be a uniform constant. A wall superheat was then defined as the temperature difference between the wall and the vapor. Since the accommodation coefficient was unknown, the maximum value of unity was chosen. The resulting film profile was a good match with experiments.

Schonberg *et al.* [24] conducted a purely numerical analysis similar to DasGupta *et al.* [30] but superheats as high as 5 K was used. They also used a Cartesian system with a single radii of

TABLE I. Summary of BC's from prior and current approaches to modeling evaporation at the transition-film region. Some manuscripts do not explicitly state all the necessary boundary conditions such as bulk curvature and values of α. The table merely represents our understanding/extrapolation from data presented in the publications.

Study	Radii of curvature	Coordinate system	Thermal BC	$\dot{m}''$ @ h_{ad}	h_{ad} BC	Guesses/tuning	h_{tr} BC	Bulk $\dot{m}_{exp}$	α
Stephan and Busse [39]	1	Cartesian	Nonuniform T_{wall}, tuned	Set to zero	Calculate from zero mass flux	Tuned all derivatives at h_{ad}	Constant curvature	No	1
DasGupta et al. [30]	1	Cartesian	Constant T_{wall}	Set to zero	Experimental	Tuning of nondimensional numbers	Experimental	No	1
Schonberg et al. [24]	1	Cartesian	Constant T_{wall}	Set to zero	Calculate from zero mass flux	Tuned all derivatives at h_{ad}	Apparent contact angle	No	1
Park et al. [31]	1	Cartesian	Constant heat flux	Set to zero	Not specified	All derivatives set to zero	Not specified	No	1
Wee et al. [32]	2	Cylindrical	Constant T_{wall}	Set to zero	Calculate from zero mass flux	Iterative tuning to match bulk	Arbitrary constant curvature		1
Wang et al. [33]	1	Cartesian	Constant T_{wall}	Set to zero	calculate from zero mass flux	$h_{ad_x} = 0$, $h_{ad_{xx}}$ tuned to match bulk	Arbitrary constant curvature	No	1
Wang et al. [34]	N/A	Cartesian	Constant T_{wall}	Set to zero	Calculate from zero mass flux	N/A	Arbitrary constant curvature	No	N/A
Plawsky et al. [35]	2	Cartesian	Constant T_{wall}	Set to zero	Experimental	Slip and h_{ad}	Experimental	No	1
Du and Zhao [43]	1	Cartesian	Constant heat flux	Set to zero	Calculate from zero mass flux	$h_{ad_x} \approx 1e-8$, $h_{ad_{xx}}$ is tuned	Arbitrary constant curvature	No	1
Kou et al. [44]	1	Cartesian	Constant T_{wall}	Set to zero	Calculate from zero mass flux	$h_{ad_x} \approx 1e-11$, $h_{ad_{xx}}$ is tuned	Arbitrary meniscus radius.	No	1
Akkuş and Dursunkaya [29]	1	Cartesian	Constant T_{wall}	Set to zero	No guesses necessary	Inlet mass flow rate at bulk	Arbitrary	No	1
Current study	2	Cylindrical	Nonuniform T_{wall}	Not constrained	No guesses necessary	$h_{ad_x} = 0$	Experimental	Yes	Calculated

curvature, a uniform and constant superheat, and an accommodation coefficient of 1. This study established that the existence of a stable evaporating meniscus at high heat flux were theoretically possible. The thin-film profile was matched to an arbitrary apparent contact angle in the thick meniscus.

Park *et al.* [31] developed a thin-film model for a constant heat flux condition at the wall. Wee *et al.* [32] used cylindrical coordinates with both radii of curvatures and included thermocapillary effects. Wee *et al.* [32] explicitly state that the solution is extremely sensitive to the physical boundary conditions. Wang *et al.* [33] built a thin-film model to investigate the effect of different flavors of the kinetic phase-change models [Eqs. (1) and (2)] on the local mass flux and found that at the results begin to deviate at superheats greater than 5 K. The same authors also developed an analytical approach to the problem by neglecting capillary and disjoining pressure [34]. Plawsky *et al.* [35] built a model similar to DasGupta *et al.* [30] but needed to use a slip velocity to get a match with an experimentally measured film profile. In most studies, three sets of boundary conditions (BC's) are needed for integrating the mass balance, energy balance, and liquid-vapor interface profile. These BC's are defined either at h_{tr} (film thickness to denote start of the transition region) and/or h_{ad} (adsorbed film thickness).

A. Mass balance BC

Mass flux BC's must be specified at both h_{tr} and h_{ad} for a unique solution. In a traditional transition-film model, the mass flux at the beginning of the transition region ($\dot{m}''$ at h_{tr}) is not known *a priori* [29]. This is due to a lack of comparison with bulk experimental data and/or multiscale modeling. Further, most models assume that the adsorbed film is nonevaporating ($\dot{m}''$ at $h_{ad} = 0$) but the validity of this assumption has recently been questioned [36]. The assumption of a nonevaporating adsorbed film along with lack of experimental data reduces $\dot{m}''$ at h_{tr} to an arbitrary, unconstrained matching point.

B. Energy balance BC

Most models use a constant temperature or constant heat flux boundary, but this is shown to be inadequate [37–39]. A constant surface temperature is usually specified as a wall superheat ($T_{wall} - T_v$).

C. Interface profile BC

The third-order evolution equation in the thin film requires three boundary conditions. The computational domain size, i.e., the length and film thickness derivatives in the transition-film region, is not known *a priori*. One approach is to start from the adsorbed film with a guessed value of h_{ad} and the corresponding film thickness derivatives (h_{ad_x}, $h_{ad_{xx}}$). The profile is then matched to a specified bulk curvature at an arbitrary length using a shooting method [24,26,27]. In order to match the bulk curvature, researchers in the past have "tuned" a combination of h_{ad} and its derivatives and/or slip length [26,27,35,40–42]. Even if a matched curvature solution may be obtained, the resulting initial conditions have a great potential to be nonphysical and/or nonunique.

The study conducted by Akkuş and Dursunkaya [29] is fundamentally unique from previous models which integrated the evolution equation from the adsorbed film and marched in the direction of the bulk meniscus. Akkuş and Dursunkaya [29] reversed the integration process. This approach begins with an initial guessed value of mass flow into the transition-film region. The set of equations describing mass, energy and momentum in the transition-film region are evaluated until $\dot{m}'' \to 0$. The film thickness at which $\dot{m}'' \to 0$ is presumed to be h_{ad}. This constraint serves as an additional boundary condition. If the film thickness and its derivatives at the thick film (h_{tr}) are known (experimentally measured), the correct mass flow into the transition region is determined iteratively. This alleviates the need for guessing multiple boundary conditions at the adsorbed film. They show

that by starting at a known point in the bulk meniscus, the model could be solved with minimal guesses to the physical boundary conditions.

Most models do not derive boundary or coupling conditions from experimental data. To the best of the authors' knowledge, no attempt has been made to validate models using an experimentally measured value of the bulk evaporation rate. A comparison to experimentally measured bulk evaporation rates requires estimation of mass flux not just in the thin film but the bulk meniscus as well. All the thin-film models built on a lubrication approximation begin to systematically introduce errors as film thickness increases. This further necessitates a need for an expansion of the thin-film model into the bulk meniscus using an alternative approach.

There are several studies that have developed an evaporation model focusing on just the bulk meniscus [45–47]. These models uniquely couple the kinetic model of phase change with a diffusive model in the vapor for a multicomponent mixture. These models do not account for curvature, disjoining pressure, or the enhanced evaporation in the transition region. The mass flux increases monotonically as the film thickness reduces and if an adsorbed film is not used, the mass flux reaches a singularity. The singularity could be alleviated by truncating the macroscale approach at the thin film and coupling it to an independent microscale model of the thin film [24].

It is difficult to develop a single modeling framework that works well at all length scales. There have been limited attempts at a coupling between the length scales and many issues are yet to be resolved [39,43,48,49]. The multiscale approach was first introduced by Stephan and Busse [39]. They used a microscale thin-film model coupled with a thermal transport model in the macroscale bulk meniscus. The solution begins with several assumptions in the microscale thin-film model. The third derivative was iterated with a perturbed value of capillary pressure. The macroscale model was then solved to determine a wall temperature that matches the total heat lost from the micromodel. During this process, the interfacial temperature was kept uniform and constant in the macroscale model. Once a match was obtained, the constant wall temperature boundary was relaxed and a wall temperature distribution as determined from the macro model was implemented. Film profile and curvature matching at the intersection of micro and macro regions was not discussed. There was no experimental validation to the coupled approach. Zheng *et al.* [48] published a multiscale model but did not report the methodology for coupling the thin-film and meniscus solutions. They also report a linear thin-film profile and slope of unity suggesting a trivial thin-film solution. Du and Zhao [43] report the coupling methodology but assume the bulk meniscus shape to be an arc of a circle that is not affected by evaporation. In a prior publication, the same authors also stated that the arc of a circle approximation is incorrect [25]. Yi *et al.* [49] state that they developed a "truly comprehensive multiscale [model]" but the coupling between the two length scales did not ensure continuity of the slope of film thickness. The most likely cause of the discontinuity is the arbitrary thermal and physical boundary conditions assumed. This corroborates with prior numerical experiments done by the current authors [50] which suggested that unphysical boundary conditions are sometimes necessary to ensure a continuity in both slope/curvature and film profiles.

In summary, sensitivity to boundary conditions is a common concern in most studies of meniscus evaporation. The exact extent to which the different regions of the meniscus contributes to the bulk phase-change rate is still unclear. Most models assume a nonevaporating adsorbed film although studies have shown that as long as there is a temperature gradient present, the adsorbed film may not be a static nonevaporating film [36,51–53]. To attain a feasible solution, most studies:

(i) solve the governing equations using multiple "guesses" for the boundary conditions at the adsorbed film (with the exception of Akkuş and Dursunkaya [29]),

(ii) match to an arbitrary curvature or film thickness in the bulk meniscus (with the exception of DasGupta *et al.* [30] and Plawsky *et al.* [35]),

(iii) impose a constant, uniform temperature or heat flux boundary at the wall (with the exception of Stephan and Busse [39]), and

(iv) impose a nonevaporating condition in the adsorbed film.

The motivation behind the current study was to investigate the nonuniformity in mass flux and interfacial temperature during steady meniscus evaporation of a cryogenic propellant. The ability to predict the rate of phase change (especially in cryostorage depots) using kinetic theory remains a challenge primarily due to the absence of accommodation coefficients (α) and the inability to computationally capture the local thermodynamics [50,54–57]. Modeling phase change in stored cryogenic propellant tanks are critical to long-term space missions. This manuscript describes a multiscale approach to determine the local, nonuniform evaporation flux from a liquid hydrogen meniscus without the need for unnecessary assumptions regarding boundary conditions and values of α. The contribution from the different interfacial regions (bulk meniscus, transition region and adsorbed film) is investigated compared to the bulk experimental value.

The multiscale approach involves a coupling between two submodels: a meniscus submodel and a transition-film submodel. The meniscus submodel covers the bulk of the liquid-vapor interface but cannot resolve the thin-film transition region close to the wall. The region close to the wall, where the film thickness is on the order of micrometers, is modeled using a transition-film model. The results from the two submodels are combined using a novel coupling that (1) eliminates the need for guessing boundary conditions at the adsorbed film, (2) uses an experimentally derived film thickness and curvature at the bulk meniscus, (3) accounts for the nonuniform wall temperature, (4) does not impose a nonevaporating condition at the adsorbed film, and (5) is validated by an experimentally measured bulk evaporation rate.

II. MULTISCALE MODEL OF PHASE CHANGE

The multiscale approach is a combination of a meniscus submodel and a transition-film submodel, delineated based on the dominant component of the normal stress at the interface (Fig. 1). A thermomechanical coupling is applied at the intersection to ensure continuity of temperature, mass flux, film profile, and film slope. The goal of the model is to determine a local evaporation flux distribution from the entire interface and probe the contribution from each region. The submodels are implemented as separate functions and a wrapper script maps the local flux on to the liquid-vapor interface. The entire multiscale model is implemented in MATLAB and the code is described in Bellur's Ph.D. dissertation [58].

A. Meniscus submodel

The meniscus submodel aims to capture the evaporation mass flux over the bulk of the interface by modeling the transport processes in the liquid. At low evaporation rates, the Rayleigh number of a liquid meniscus is well below the critical Rayleigh number for natural convection and the Peclet number is <1. In this case, the heat transport to the interface is dominated by conduction in the liquid. In the case of a slow and steady meniscus evaporation with a known Bond number (Bo), the heat transport can be considered to be quasisteady.

Evaporation at the liquid-vapor interface results in localized cooling of the liquid [Eq. (3)]:

$$Q_i'' = -h_{\text{fg}}(T_i)\dot{m}''(T_i), \tag{3}$$

where Q_i'' is the heat flux due to evaporation and $\dot{m}''$ is the mass flux described by Eq. (2).

If the temperature at the wall (solid-liquid interface) temperature is known, then the liquid-vapor temperature distribution and the local evaporative mass flux could be determined using Eqs. (2) and (3).

Using the liquid-vapor interface shape from a Young-Laplace fit to a given Bond number (Bo) and contact angle (θ), a 2D axisymmetric steady-state heat conduction problem was solved using a finite-element method. A uniform mesh with 2-μm triangular elements is used as a compromise between speed and resolution. Figure 2 shows the boundary conditions used in the meniscus submodel.

Moving along the interface from the bulk meniscus to the adsorbed region, the resistance to heat transfer in the liquid is reduced. This results in an increase in interfacial temperature. An increased
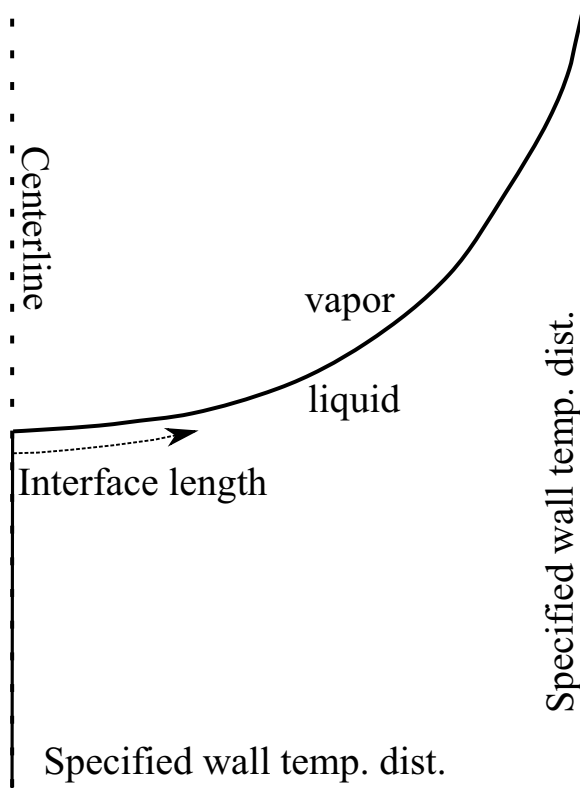
FIG. 2. Geometry and boundary conditions for the meniscus submodel.

interfacial temperature, relative to T_{sat} results in an increase in local evaporation flux [Eq. (2)]. If a perfectly wetting fluid modeled with contact angle (θ) of zero, then mass flux at the contact point reaches a singularity due to the absence of the adsorbed film. If the Young-Laplace fit is terminated at an assumed value of adsorbed film thickness, then an extremely fine mesh must be resolved. The modeling results are sensitive to the assumed adsorbed film thickness as evidenced by past studies. Without an adsorbed film, the problem is inherently mesh dependent. As the mesh is refined, the temperature peak close to the wall increases. Further, the Young-Laplace fit is not accurate at submicron thicknesses. When the liquid-vapor interface is in close proximity to the solid-liquid interface, disjoining pressure alters the local pressure field, thereby altering both the mechanical stress balance (interface shape) and the local evaporation flux. Hence, the meniscus model is not suited for evaluation at close to the wall and a secondary model is necessary to investigate evaporation in the transition-film region. The meniscus submodel must be truncated at h_{tr} to avoid errors. A simple method to effectively choose an appropriate value of h_{tr} is discussed in a later section.

B. Transition-film submodel

While the meniscus submodel accounts for evaporation in the bulk of the interface, the transition-film submodel aims to bridge the gap from the beginning of the transition region ($\approx\mu$m) to the adsorbed thin film ($\approx$nm) as shown in Fig. 1. To compute local evaporation fluxes from the transition region, a description of the micro- to nanoscale film profile is required. The film profile plays a major role in the local mass flux predicted by Eq. (2) since T_i, κ, and Π are all inherently coupled and dependent on the local film profile. Film thickness profiles at this length scale are not accessible

through traditional imaging, and hence the film profile must be computed based on mathematical modeling.

The mechanical pressure balance in the thin film can be modeled using the augmented Young-Laplace equation that accounts for both the curvature and the disjoining pressure. Equation (4), developed by DasGupta *et al.* [59], describes the local pressure jump across the liquid-vapor interface,

$$p_v - p_l = \sigma\kappa + \Pi. \tag{4}$$

Here p_v is the pressure in the vapor phase and p_l is the pressure in the liquid phase. The fluid properties and local pressure in the vapor could be assumed to be uniform and constant throughout the domain resulting in a change in liquid pressure that could be expressed explicitly in terms of curvature, κ and the disjoining pressure, Π, which are in turn dependent on local liquid-film thickness.

The geometry of interest has two planes of curvature, one due to the meniscus and the other due to the radius of the container. The geometric curvature at any location on the liquid vapor interface is

$$\kappa = (r - h)^{-1}\left(1 + h_x^2\right)^{-1/2} + h_{xx}\left(1 + h_x^2\right)^{-3/2}, \tag{5}$$

where κ is the curvature, h is the liquid-film thickness, h_x is the first derivative, h_{xx} is the second derivative, and x is the vertical distance along the solid wall.

The disjoining pressure is modeled using Eq. (6) considering only the intermolecular London-Van Der Waals forces [18],

$$\Pi = \frac{A}{h^3}, \tag{6}$$

where Π is the disjoining pressure and A is the Hamaker constant. Typical values of A constant for different fluids are between 10^{-19} to 10^{-22} J. In this work, Eq. (6) is used with $A = 5.11 \times 10^{-21}$ [60].

A steady nonlinear thin-film evolution equation as described by Eq. (7) is obtained by substituting Eqs. (5) and (6) into Eq. (4) and taking another derivative,

$$h_{xxx} - \frac{3h_{xx}^2 h_x}{1 + h_x^2} - \frac{h_{xx}h_x}{(r_{ij} - h)^2} + \frac{h_x\left(1 + h_x^2\right)}{(r_{ij} - h)^2}$$

$$+ \frac{\gamma}{\sigma}\left(\frac{1 + h_x^2}{r_{ij} - h} + h_{xx}\right)\frac{dT}{dx} + \frac{1}{\sigma}\left(1 + h_x^2\right)^{\frac{1}{2}}\left(\frac{dp_l}{dx} + \frac{d\Pi}{dx}\right) = 0. \tag{7}$$

Liquid flow in the transition film (Fig. 1) is modeled using a lubrication approximation of the Navier-Stokes equation in cylindrical coordinates,

$$\frac{1}{r}\frac{\partial}{\partial r}\left(r\frac{\partial u}{\partial r}\right) = \frac{1}{\mu_l}\frac{dp_l}{dx}, \tag{8}$$

where μ_l is the viscosity of the liquid, u is velocity, r is the local radius, and dp_l/dx is the pressure gradient along the solid wall. The equation is solved by applying a no-slip boundary condition at the wall and a tangential stress boundary condition at the interface. A temperature-dependent surface tension is used to account for Marangoni effects:

$$\text{at } r = R, \qquad u = 0$$

$$\text{at } r = R - h, \quad -\mu\frac{\partial u}{\partial r}\Big|_{r=R-h} = \frac{d\sigma}{dx},$$

where R is the radius of the test cell. On solving Eq. (8) using the given boundary conditions, an expression for velocity, $u(r)$, is obtained. The mass flow rate through a control volume ($\dot{m}_{cv}$) in the

transition-film region is

$$\dot{m}_{cv} = \int_{R-h}^{R} \rho_l u(r) 2\pi r dr. \tag{9}$$

The difference in the mass flow rate entering and exiting the control volume is set equal to the evaporative flux evaluated using the kinetic model [Eq. (2)]. From this balance, the pressure gradient dp_l/dx is obtained.

An energy balance on same transition film control volume is

$$k_l \frac{\partial}{\partial r} \left(r \frac{\partial T}{\partial r} \right) = 0. \tag{10}$$

A specified temperature boundary condition at the solid wall along with a heat flux boundary condition at the liquid-vapor interface is used to solve Eq. (10). A refined solid-fluid interface temperature distribution obtained from the previously described meniscus submodel is implemented via a cubic spline fit assuming $T_{wall} = T_v$ in the adsorbed film. The heat flux boundary condition at the interface accounts for the heat lost due to evaporation,

$$\text{at } r = R, \qquad T_{wall}(x) \text{ from meniscus submodel}$$

$$\text{at } r = R - h, \quad k_l \frac{dT}{dr} = \dot{m}'' h_{fg}.$$

Integrating Eq. (10) from wall, R, to the interface, $R - h(x)$, the interfacial temperature distribution is obtained,

$$T_i(x) = -\frac{h_{fg}}{k_l}[R - h(x)] \ln\left(\frac{R}{R-h}\right)\dot{m}'' + T_{wall}(x), \tag{11}$$

where $\dot{m}''$ is evaluated using Eq. (2).

Equations (2), (4)–(7), (9), and (11) must be evaluated numerically between the end of the bulk meniscus (h_{tr}) to the adsorbed film region (h_{ad}) as shown in Fig. 1.

In this work, a wall temperature distribution, $T_{wall}(x)$ is specified. The adsorbed film is not assumed to be an equilibrium nonevaporating film. A modified version of the methodology proposed by Akkuş and Dursunkaya [29] is used to evaluate the transition-film submodel. The values of the derivatives at h_{tr} (h_x and h_{xx}) are determined the Young-Laplace fit. $\dot{m}''$ and T_i at h_{tr} is known from the truncated meniscus model and serves as additional initial conditions. The explicit specification of all quantities at h_{tr} ensures continuity of film, evaporative mass flux, and interface temperature profiles between the two submodels and avoids a need for "matching." The transition-film submodel [Eqs. (2), (4)–(7), (9) and (11)] is evaluated in the direction of reducing film thickness until the local value of h_x reaches zero. The adsorbed film is presumed to be a flat film with a slope of zero. The film is not set to be nonevaporating but depends on the local thermomechanical contributions to phase change [$T_{wall}(x)$, Π, Bo, or κ and θ].

In summary, the multiscale modeling methodology starts in the bulk region based on a Young-Laplace fit and terminates in an adsorbed film whose thickness and mass flux is not known *a priori*. Four inputs are necessary to evaluate the model: (1) Bond number, Bo; (2) contact angle, θ; (3) wall temperature distribution, $T_{wall}(x)$; and (4) vapor pressure (p_v). Bo and θ define bulk curvature. The wall temperature distribution and vapor pressure are the boundary conditions for the computational domain. Data from the authors' NIST cryoneutron phase-change experiments were used to determine the boundary conditions.

III. NEUTRON IMAGING EXPERIMENTS

Phase-change experiments with cryogenic propellants were conducted in the BT-2 neutron imaging facility at the NIST Center for Neutron Research in Gaithersburg, MD. The large variation

in neutron attenuation between metals and the cryogenic propellants allow for visualization of the liquid/vapor mixture inside opaque metallic containers [54,61]. Cylindrical test cells of different sizes (10-mm and 30-mm diameters) and materials (Al 6061 and SS 316) were used in the experiments to test changes in both surface chemistry and curvature. By controlling both temperature and pressure, a range of phase-change rates were observed at various thermodynamic conditions. The vapor pressure was kept constant during each test run and temperature is varied from T_{sat} to induce condensation and/or evaporation. Figure 3(a) shows time-lapse images captured at 121 kPa in the 10-mm Al cell and Fig. 3(b) shows the corresponding liquid volume. Images 1–4 of Fig. 3(a) show condensation of liquid hydrogen and images 4–8 show subsequent evaporation. There was no observable hysteresis in the shape of the liquid vapor interface. Liquid hydrogen perfectly wetted both Al 6061 and SS 316 cells ($\theta = 0°$ [61]). Additional detail on the experiment setup, neutron image analysis, bulk evaporation rate ($\dot{m}_{exp}$), and cryostat operation is detailed in the authors' previous publications [50,54,61–65].

Due to the nature of the experiments, temperature could be measured only along a few discrete locations on the outer wall of the test cells [Fig. 3(a)]. In order to extract the inner-wall solid-fluid interface distribution $T_{wall}(x)$ from outer-wall experimental data, a thermal transport model has already been built and validated with experimental data. Details on the thermal model and the determination of the solid-fluid interface temperature distribution can be found in Bellur *et al.* [66].

IV. MULTISCALE MODEL WITH EXPERIMENTAL INPUTS

The low evaporation rates measured in the experiments combined with geometry of the test cell suggest that the Rayleigh number was well within the critical Rayleigh number for natural convection and the Peclet number is estimated to be less than 10^{-2}. The conductivity of liquid hydrogen is an order of magnitude greater than that of it's vapor. Evaporation results in a bulk movement of vapor molecules upward from the interface toward the outlet at the top of the test cell. Heat transfer to the interface is primarily by conduction in the liquid. Since the evaporation rate is low, the liquid-vapor mixture could be considered quasisteady and a steady-state model was implemented with a fixed liquid-vapor interface.

The multiscale model begins with evaluation of the meniscus submodel. A Young-Laplace fit to the liquid-vapor interface from the neutron images and the location of the meniscus apex is used to model a static liquid-vapor interface. The wall temperature distribution $T_{wall}(x)$ obtained from the previously published thermal transport model [66] is used an input along with Eq. (2) at the liquid-vapor interface. Figure 4 shows the variation in both mass flux and temperature along the interface, starting at the apex of the meniscus and truncated at a film thickness of 10 μm. This film thickness was chosen as the truncation point since this is within the optical resolution from neutron imaging. The film thickness, its derivatives and local curvature at this point could be determined experimentally. An efficient method to verify the choice of h_{tr} is to ensure the ratio of disjoining pressure to capillary pressure is $<10^{-3}$ and the Young-Laplace fit is still valid.

In the bulk meniscus, the interfacial temperatures remain fairly constant and close to T_{sat}, which was experimentally determined from the pressure measurement to be 20.99 ± 0.015 K. The curvature of the liquid vapor interface is inversely proportional to the film thickness. As a result, the increasing curvature in the transition film causes a decrease in local evaporation flux toward the adsorbed film [Eq. (2)]. The mechanical contribution to evaporation flux (curvature and disjoining pressure) is usually negligible in comparison to the thermal contribution in the bulk meniscus. For this reason, mass flux in Fig. 4 is directly related to interfacial temperature through Eq. (2). In the evaporation experiments with the 10-mm Al cell, the local superheat is low (<0.1 K) and the Bond number is approximately 9.8, and ignoring the curvature and disjoining pressure effects in the bulk meniscus varies the local mass flux less than 0.1%.

$\dot{m}''$ and T_i at h_{tr} are then used to evaluate the transition-film submodel starting at h_{tr} and terminated at h_{ad}. Figure 5 shows the film profile obtained as a result of the transition-film model for a 10-mm Al cell containing hydrogen evaporating at 121.3 kPa with $\alpha = 0.45$. In Fig. 5, the
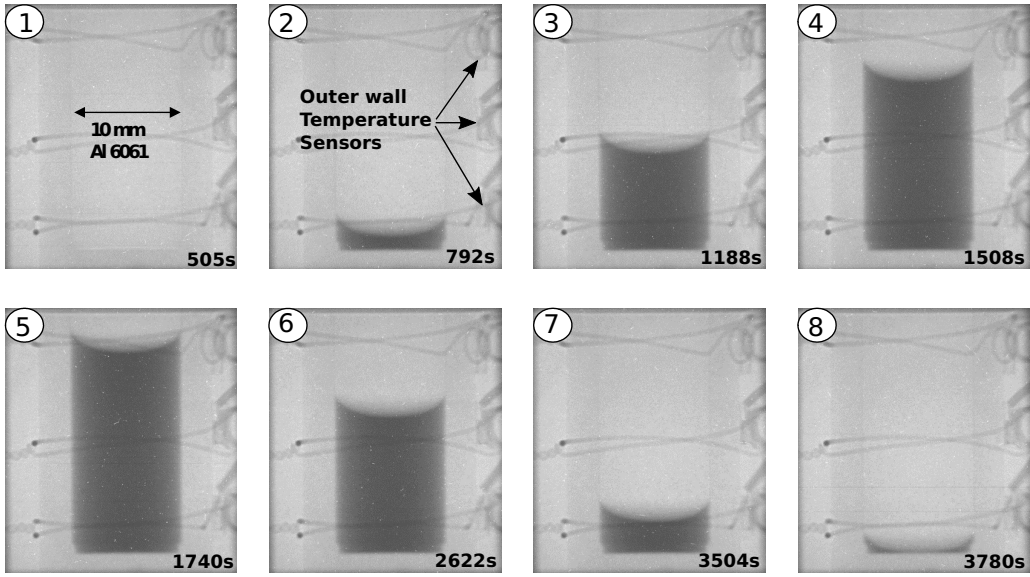
(a) Time lapse images
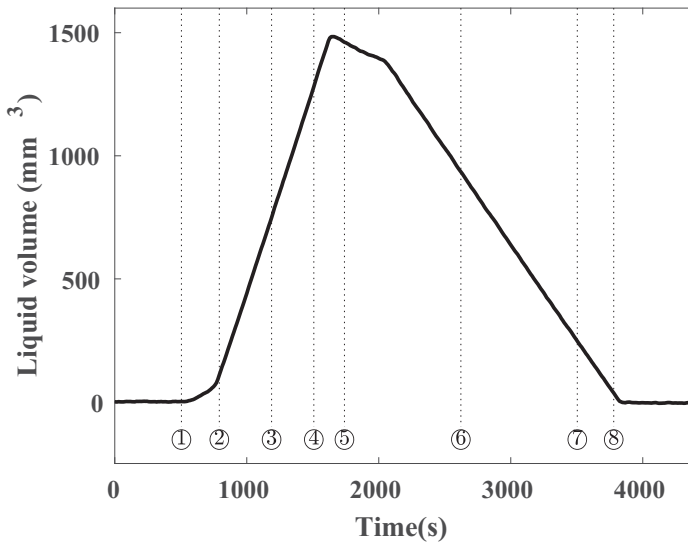
(b) Liquid volume

FIG. 3. Sample images (a) and calculated liquid volume (b) from an evaporation/condensation test with saturated hydrogen at 120.9 kPa in the 10-mm Al cell; Bo = 9.8 and $\theta = 0$ [61]. Images 1–4 show condensation and images 5–8 show evaporation. The phase-change rates were calculated by linear fits to the corresponding regions on the volume vs. time plot.

origin corresponds to the solid-liquid interface at a film thickness of 10 μm. As the film thickness decreases, the modeling results deviate from the Young-Laplace fit, which is valid only in the bulk meniscus region. The inset of Fig. 5 shows the model ending in an adsorbed film while the Young-Laplace fit ends in a zero film thickness. Once $h_x = 0$ is obtained, solution of the evolution
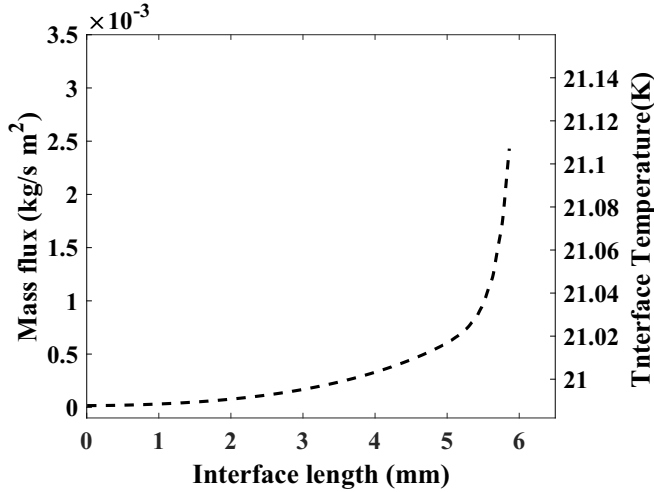
FIG. 4. Local interfacial temperature and mass flux along the liquid-vapor interface from the meniscus submodel. Zero value on the x axis refers to the apex of the meniscus as shown in Figs. 1 and 2. Results for film thickness <10 μm are neglected.

equation in the thin film is terminated. The film thickness at which $h_x = 0$ is presumed to be h_{ad}. An adsorbed film thickness of approximately 20 nm is observed.

The film profile is then used to evaluate the local mass flux profile using Eq. (2). Thermal contribution to phase change [first term in Eq. (2)] is at least three orders of magnitude greater than the mechanical contribution to phase change [second term in Eq. (2)] at h_{tr}. The ratio decreases and ultimately approaches unity as the film thickness decreases. Figure 6 shows the variation in local evaporative mass flux ($\dot{m}''$) and wall temperature (T_{wall}) along the transition film. The termination
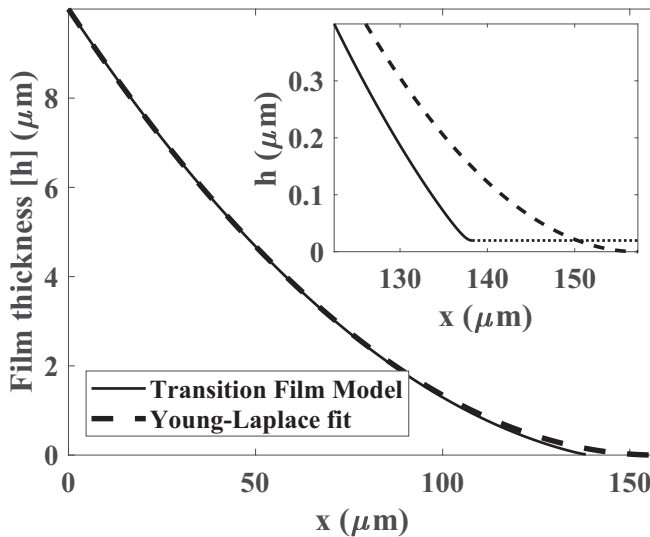
FIG. 5. Transition-film profile in a 10-mm Al cell containing hydrogen evaporating at 121.3 kPa, $\alpha = 0.45$. The origin corresponds to the liquid-solid interface at a film thickness of 10 μm and x is along the solid-liquid interface.
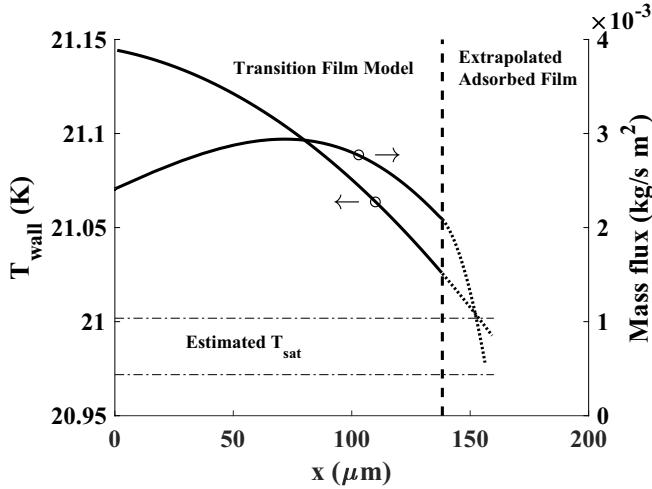
FIG. 6. Mass flux and wall temperature profiles in a 10-mm Al cell containing hydrogen evaporating at 121.3 kPa, $\alpha = 0.45$. The origin corresponds to the liquid-solid interface at a film thickness of 10 μm, and x is along the solid-liquid interface. The solution of the transition-film submodel is terminated at $h_x = 0$, indicated by the vertical dashed line. Mass flux is extrapolated another 10 μm from the location where $h_x = 0$ under the assumption that the liquid film remains flat. Extrapolated mass flux and wall temperature are shown with dotted lines. The mass flux in the adsorbed film must approach zero. The wall temperature will reach a minimum and then increase when there is no longer any mass flux as suggested by the macroscale thermal transport model [66].

of the transition-film model at $h_x = 0$ is represented by the dashed vertical line. Evaporative mass flux at the adsorbed film ($\dot{m}''$ at h_{ad}) is not constrained to be zero but rather depends on the local thermomechanical contributions [Eq. (2)].

The multiscale methodology is summarized in Fig. 7(a) and the combined mass flux distribution from the model is shown in Fig. 7(b). The origin in Fig. 7(b) corresponds to the apex of the meniscus. Moving along the interface away from the apex represents an increasing interface length and a decreasing film thickness. Both the film and mass flux profiles are continuous and smooth at the submodel coupling point (h_{tr}). The combined solution exhibits a peak in mass flux in the transition-film region. At film thicknesses close to h_{ad} the mass flux drops. The peak flux in the transition region is almost two orders of magnitude greater than the flux at the apex of the meniscus.

Assuming a perfectly flat film ($h_x = h_{xx} = 0$) in the adsorbed region, Eq. (2) is evaluated resulting in an extrapolation into the adsorbed region. This region is shown by dotted curves in Figs. 5 and 6 and is only representative of the expected trend but not a true solution for two reasons: (1) Adsorbed film is probably not a steady, flat film but rather dynamic with possible periodic oscillations [51] and (2) there is a high degree of uncertainty in estimation of T_{wall} at film thickness below 2 μm (meniscus-scale model resolution). Here a cubic spline extrapolation is used assuming minimum[$T_{wall}(x)$] = T_v. Further, the estimation is based on the Young-Laplace fit which overestimates the length of the transition-film region. As a result, in the transition-film model, T_{wall} at h_{ad} is greater than T_v. This is also a possible reason why the evaporative mass flux at the adsorbed $\dot{m}''_{ad} \neq 0$. MD results further suggest that as long as there is a temperature gradient in the solid, there is the possibility that adsorbed films are not necessarily regions of zero interfacial mass transfer [36]. Advances in high-resolution experimental techniques to measure sub-micron-scale solid temperature profiles are necessary to gain a better understanding of the thermofluid transport in the vicinity of the adsorbed film. T_{wall} most likely exhibits a minimum in the adsorbed film and

(a) Multiscale methodology

(b) Combined local mass flux
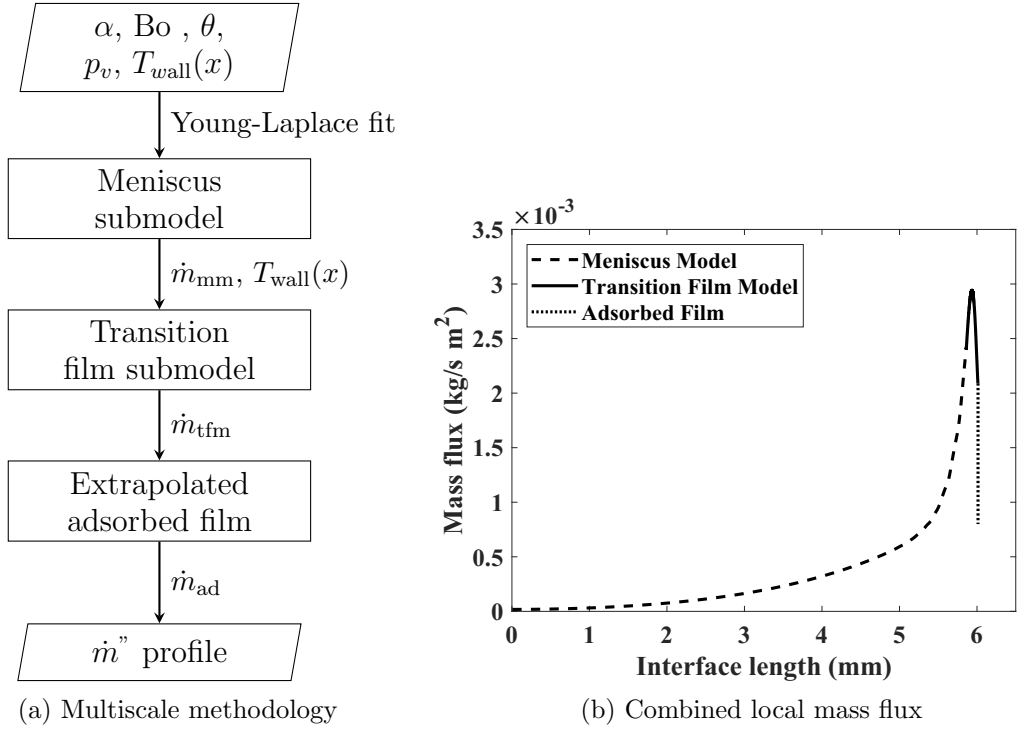
FIG. 7. Methodology (a) and combined mass flux values (b) from the coupled multiscale model for a 10-mm Al cell containing hydrogen evaporating at 121.3 kPa, $\alpha = 0.45$.

increases with further increase in x [66]. The location of this minimum is close but not necessarily equivalent to the location the peak evaporative flux.

The multiscale model is used with evaporation data from three different test cells and at vapor pressures between 88 and 226 kPa. From each case, the local mass flux profile from each of the submodels is integrated over the corresponding interfacial area to obtain $\dot{m}_{mm}$ and $\dot{m}_{tfm}$ and $\dot{m}_{ad}$. Table II summarizes the data from the liquid hydrogen tests with 10 mm Al, 10-mm SS and 30-mm Al cells at different saturation vapor pressures using $h_{tr} = 10\ \mu$m. The contribution from the bulk meniscus, $\dot{m}_{mm}$, is between 78 and 95% of $\dot{m}_{exp}$ and varies with test cell size, material, and pressure:

TABLE II. Multimodeling results with different experimental inputs. $\dot{m}$ values are in μg/s.

Test cell	Area (mm^2)	Perimeter (mm)	Pressure (kPa)	$\dot{m}_{exp}$	$\dot{m}_{mm}$	$\dot{m}_{tfm}$	$\dot{m}_{ad}$	$\frac{\dot{m}_{mm}}{\dot{m}_{exp}}$
10 mm SS	107.92	31.4	88.32	17.27	14.72	2.49	0.06	0.852
			120.9	16.43	14.17	2.25	0.01	0.862
			201.96	21.39	18.54	2.84	0.01	0.866
			218.92	76.31	67.04	9.25	0.02	0.878
30 mm Al	798.09	94.2	121.94	102.70	97.66	4.97	0.07	0.950
10 mm Al	107.92	31.4	87.9	55.20	43.44	11.75	0.01	0.787
			121.3	55.50	43.74	11.18	0.08	0.788
			200.05	93.12	73.89	19.22	0.01	0.793
			226.84	77.31	62.85	14.47	0.01	0.813
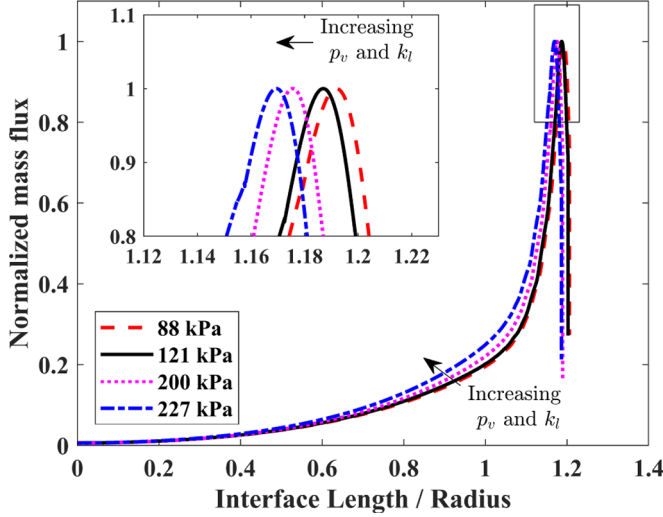
FIG. 8. Normalized mass flux distribution with pressure for hydrogen tests with the 10-mm Al cell. Vapor pressure was controlled in the experiments a manifold. Refer to Table II for integrated evaporation rate values delineated by region.

A. Size

As the diameter of the cell was increased from 10 to 30 mm, $\frac{\dot{m}_{mm}}{\dot{m}_{exp}}$ increases from 0.788 to 0.950 with the same wall material and equivalent vapor pressure. This finding supports the commonly accepted hypothesis that thin film contribution is reduced as Bo or the ratio of surface area to contact line length is increased.

B. Pressure

The bulk meniscus contribution increases with increasing pressure for both SS and Al cells, suggesting that the local mass flux profile shifts toward the bulk meniscus at higher pressures. Figure 8 shows the variation in mass flux with vapor pressure for the 10-mm Al cell tests. The mass flux was normalized with the peak value for each case so that tests with different bulk evaporation rates could be compared. The interface length was normalized with test cell radius. The systemic shift in the peak toward the bulk meniscus causes an increase in the value of $\frac{\dot{m}_{mm}}{\dot{m}_{exp}}$ with pressure for the same test cell. This trend is most likely due to an increase in liquid thermal conductivity with pressure: 0.1 W/m-K at 88 kPa to 0.22 W/m-K at 220 kPa.

C. Material

Values of $\frac{\dot{m}_{mm}}{\dot{m}_{exp}}$ for the SS cell are about 7–8% greater than similar values for the Al cell, suggesting that the heat transport in the solid effects the mass flux profile considerably. A substrate with higher thermal conductivity (Al) has an increased potential for sustaining thin film evaporation and hence a lower value of $\frac{\dot{m}_{mm}}{\dot{m}_{exp}}$.

The effect of evaporation rate or wall superheat on $\frac{\dot{m}_{mm}}{\dot{m}_{exp}}$ is negligible. $\dot{m}_{ad}$ is generally <3% of $\dot{m}_{tfm}$ and 0.1% of $\dot{m}_{exp}$. In the results shown, level of confidence in the value of $\dot{m}_{ad}$ is poor and assuming a nonevaporating adsorbed film may be appropriate when modeling macroscale evaporation. However, the assumption may introduce errors when the length scales of interest are <1 μm or Bo <1.

The adsorbed film thickness obtained is sensitive to the model of disjoining pressure used and the local wall temperature distribution in the facility of the adsorbed film. The adsorbed film thickness also varies with the experimental test conditions and the geometry of the test cell but lies between 17 and 22 nm for the set of conditions simulated. A varying the value of the Hamakar constant by up to an order of magnitude results in $<5\%$ variation in $\dot{m}_{\mathrm{tfm}}$. Further work is necessary to investigate the effect of different disjoining pressure models and experimental conditions on the value of h_{ad}.

α for a given test condition could be determined by comparing the modeling results with a measured bulk rate. The values of α used in this work and the methodology is the topic of a forthcoming paper.

V. SUMMARY AND CONCLUSION

A complete description of evaporation at a curved liquid vapor interface such as that from a meniscus is important in fields. The problem is compounded by the fact that there are several different length scales that effect phase change and most of the modeling in the past has either focused on the transition film or the bulk meniscus. Further, several simplifying assumptions or tuning parameters are necessary in order to obtain a feasible solution. Further, the value of the accommodation coefficient (α) is often assumed to be the theoretical maximum, unity, even though there are several discrepancies [3,14,15]. Coupling the different scales especially with experimental data has been a challenge. A multiscale approach to model the local, nonuniform evaporation flux in a steady meniscus is provided.

The multiscale model comprises of a macroscale meniscus submodel (to describe phase change along the bulk of the liquid vapor interface) and a microscale transition film submodel (to account for the enhanced evaporation flux close to the wall). The results from the two submodels are coupled to develop a multiscale methodology that (1) is devoid of guesses for boundary conditions at the adsorbed film, (2) uses an experimentally derived film thickness and curvature at the bulk meniscus, (3) accounts for the nonuniform wall temperature, (4) does not impose a nonevaporating condition at the adsorbed film, and (5) is validated by an experimentally measured bulk evaporation rate.

The multiscale modeling results suggest that starting from the meniscus scale and then integrating the transition film model down to the adsorbed film alleviates the need for "guessing" or "tuning" several sensitive boundary conditions at the adsorbed film. Starting from a bulk meniscus also has the added advantage of the ability to start with an experimentally obtainable (with relative ease) film thickness, curvature, interfacial temperature, and mass flux. This ensures, by default, a continuity in the film and mass flux profiles. The conditions at the adsorbed film are not known *a priori* but are a natural solution to the governing equations. The model requires α, Bo, θ, p_v, $T_{\mathrm{wall}}(x)$ as inputs and generates a smooth multiscale description of the local evaporation flux along the liquid-vapor interface.

The multiscale model is evaluated with inputs from the cryoneutron experiments conducted at the National Institute of Standards and Technology (NIST) [54] and the conclusions are summarized:

(i) The peak evaporative flux in the transition region is almost two orders of magnitude greater than the flux at the apex of the meniscus.

(ii) When the local evaporative flux is integrated over the interfacial area, evaporation from the bulk meniscus accounts for 78–95% of the total evaporation rate. This value is inherently dependent on the cutoff used to delineate the bulk region from the transition region. Here a film thickness value of 10 μm (h_{tr}) is used.

(iii) The bulk meniscus contribution increases with increase in pressure and Bo.

(iv) The bulk meniscus contribution decreases with an increase in thermal conductivity of the substrate.

(v) Evaporation from the adsorbed film is approximately 0.1% of the bulk evaporation rate. If Bo is high, assuming a nonevaporating adsorbed film may be appropriate but as Bo reduces, then the assumption may introduce errors depending on the local thermal profile in the adsorbed film.

Thermospatial resolution is a limiting factor that needs to be addressed in future studies as phase change on adsorbed films have the potential to manifest as macroscale interfacial instabilities.

(vi) Using the multiscale methodology in conjunction with an experimentally measured bulk rate, the value of α could be determined explicitly. This alleviates the need for yet another assumption/tuning parameter in most models. A discussion of α for hydrogen and methane is the topic of a forthcoming manuscript.

ACKNOWLEDGMENTS

[1] C. E. Kolb, R. A. Cox, J. P. D. Abbatt, M. Ammann, E. J. Davis, D. J. Donaldson, B. C. Garrett, C. George, P. T. Griffiths, D. R. Hanson, M. Kulmala, G. McFiggans, U. Pöschl, I. Riipinen, M. J. Rossi, Y. Rudich, P. E. Wagner, P. M. Winkler, D. R. Worsnop, and C. D. O' Dowd, An overview of current issues in the uptake of atmospheric trace gases by aerosols and clouds, Atmos. Chem. Phys. **10**, 10561 (2010).

[2] H. R. Pruppacher and J. D. Klett, *Microphysics of Clouds and Precipitation* (Springer Netherlands, Amsterdam, 2010).

[3] M. Mozurkewich, Aerosol growth and the condensation coefficient for water: A review, Aerosol Sci. Technol. **5**, 223 (1986).

[4] B. Paul, Compilation of evaporation coefficients, ARS J. **32**, 1321 (1962).

[5] D. Singh, X. Guo, A. Alexeenko, J. Y. Murthy, and T. S. Fisher, Modeling of subcontinuum thermal transport across semiconductor-gas interfaces, J. Appl. Phys. **106**, 024314 (2009).

[6] V. P. Carey, G. Chen, C. Grigoropoulos, M. Kaviany, and A. Majumdar, A review of heat transfer physics, Nanosc. Microsc. Thermophys. Eng. **12**, 1 (2008).

[7] D. Bayer, U. Gross, and K. Raed, A new facility for the experimental investigation on nano heat transfer between gas molecules and ceramic surfaces, in *Proceedings of the 32nd International Thermal Conductivity Conference* (Purdue University, West Lafayette, Indiana, USA, 2014).

[8] National Research Council, *NASA Space Technology Roadmaps and Priorities* (National Academies Press, Washington, DC, 2012).

[9] D. Brutin and V. Starov, Recent advances in droplet wetting and evaporation, Chem. Soc. Rev. **47**, 558 (2018).

[10] M. A. Saxton, D. Vella, J. P. Whiteley, and J. M. Oliver, Kinetic effects regularize the mass-flux singularity at the contact line of a thin evaporating drop, J. Eng. Math. **106**, 47 (2017).

[11] R. W. Schrage, A theoretical study of interphase mass transfer, Ph.D. thesis, Columbia University Press, 1953.

[12] J. Barrett and C. Clement, Kinetic evaporation and condensation rates and their coefficients, J. Colloid Interface Sci. **150**, 352 (1992).

[13] V. S. Ajaev, *Interfacial Fluid Mechanics* (Springer US, New York, 2012).

[14] E. J. Davis, A history and state-of-the-art of accommodation coefficients, Atmos. Res. **82**, 561 (2006).

[15] R. Marek and J. Straub, Analysis of the evaporation coefficient and the condensation coefficient of water, Int. J. Heat Mass Transf. **44**, 39 (2001).

[16] P. Davidovits, C. E. Kolb, L. R. Williams, J. T. Jayne, and D. R. Worsnop, Update 1 of: Mass accommodation and chemical reactions at gas-liquid interfaces, Chem. Rev. **111**, 1323 (2011).

[17] A. H. Persad and C. A. Ward, Expressions for the evaporation and condensation coefficients in the hertz-knudsen relation, Chem. Rev. **116**, 7727 (2016).

[18] P. C. Wayner, Y. K. Kao, and L. V. LaCroix, The interline heat-transfer coefficient of an evaporating wetting film, Int. J. Heat Mass Transf. **19**, 487 (1976).

[19] J. L. Plawsky, M. Ojha, A. Chatterjee, and P. C. Wayner, Review of the effects of surface topography, surface chemistry, and fluid physics on evaporation at the contact line, Chem. Eng. Commun. **196**, 658 (2008).

[20] P. C. Wayner, The effect of interfacial mass transport on flow in thin liquid films, Colloids Surf. **52**, 71 (1991).

[21] M. Potash and P. C. Wayner, Evaporation from a two-dimensional extended meniscus, Int. J. Heat Mass Transf. **15**, 1851 (1972).

[22] S. DasGupta, I. Y. Kim, and P. C. Wayner, Use of the kelvin-clapeyron equation to model an evaporating curved microfilm, J. Heat Transfer **116**, 1007 (1994).

[23] F. W. Holm and S. P. Goplen, Heat transfer in the meniscus thin-film transition region, J. Heat Transfer **101**, 543 (1979).

[24] J. A. Schonberg, S. DasGupta, and P. C. Wayner, An augmented young-laplace model of an evaporating meniscus in a microchannel with high heat flux, Exp. Therm. Fluid Sci. **10**, 163 (1995).

[25] Shi-Yuan Du and Yao-Hua Zhao, New boundary conditions for the evaporating thin-film model in a rectangular micro channel, Int. J. Heat Mass Transf. **54**, 3694 (2011).

[26] S.-K. Wee, K. D. Kihm, D. M. Pratt, and J. S. Allen, Microscale heat and mass transport of evaporating thin film of binary mixture, J. Thermophys. Heat Transf. **20**, 320 (2006).

[27] D. L Fritz, Implementation of a phenomenological evaporation model into a porous network simulation for water management in low temperature fuel cells, Ph.D. thesis, Michigan Technological University, 2012.

[28] V. S. Ajaev and O. A. Kabov, Heat and mass transfer near contact lines on heated surfaces, Int. J. Heat Mass Transf. **108**, 918 (2017).

[29] Y. Akkuş and Z. Dursunkaya, A new approach to thin film evaporation modeling, Int. J. Heat Mass Transf. **101**, 742 (2016).

[30] S. DasGupta, J. A. Schonberg, I. Y. Kim, and P. C. Wayner, Use of the augmented young-laplace equation to model equilibrium and evaporating extended menisci, J. Colloid Interface Sci. **157**, 332 (1993).

[31] K. Park, K.-J. Noh, and K.-S. Lee, Transport phenomena in the thin-film region of a micro-channel, Int. J. Heat Mass Transf. **46**, 2381 (2003).

[32] S.-K. Wee, K. D. Kihm, and K. P. Hallinan, Effects of the liquid polarity and the wall slip on the heat and mass transport characteristics of the micro-scale evaporating transition film, Int. J. Heat Mass Transf. **48**, 265 (2005).

[33] H. Wang, S. V. Garimella, and J. Y. Murthy, Characteristics of an evaporating thin film in a microchannel, Int. J. Heat Mass Transf. **50**, 3933 (2007).

[34] H. Wang, S. V. Garimella, and J. Y. Murthy, An analytical solution for the total heat transfer in the thin-film region of an evaporating meniscus, Int. J. Heat Mass Transf. **51**, 6317 (2008).

[35] J. L. Plawsky, A. Chatterjee, and P. C. Wayner, Jr., Modeling conact line dynamics in evaporating menisci, in *Proceedings of the COMSOL Conference 2009 Boston 2009 Comsol User's Conference* (COMSOL, Boston, MA, USA, 2009).

[36] Y. Akkus, A. Koklu, and A. Beskok, Atomic scale interfacial transport at an extended evaporating meniscus, Langmuir **35**, 4491 (2019).

[37] V. S. Ajaev and E. Ya Gatapova, Contact line motion over heated substrates with spatially nonuniform wetting properties, J. Phys.: Conf. Ser. **925**, 012016 (2017).

[38] C. Sodtke, V. S. Ajaev, and P. Stephan, Dynamics of volatile liquid droplets on heated surfaces: Theory versus experiment, J. Fluid Mech. **610**, 343 (2008).

[39] P. C. Stephan and C. A. Busse, Analysis of the heat transfer coefficient of grooved heat pipe evaporator walls, Int. J. Heat Mass Transf. **35**, 383 (1992).

[40] S. S. Panchamgam, A. Chatterjee, J. L. Plawsky, and P. C. Wayner, Comprehensive experimental and theoretical study of fluid flow and heat transfer in a microscopic evaporating meniscus in a miniature heat exchanger, Int. J. Heat Mass Transf. **51**, 5368 (2008).

[41] L. Biswal, S. K. Som, and S. Chakraborty, Thin film evaporation in microchannels with slope- and curvature-dependent disjoining pressure, Int. J. Heat Mass Transf. **57**, 402 (2013).

[42] M. S. Hanchak, M. D. Vangsness, L. W. Byrd, and J. S. Ervin, Thin film evaporation of n-octane on silicon: Experiments and theory, Int. J. Heat Mass Transf. **75**, 196 (2014).

[43] Shi-Yuan Du and Yao-Hua Zhao, Numerical study of conjugated heat transfer in evaporating thin-films near the contact line, Int. J. Heat Mass Transf. **55**, 61 (2012).

[44] Zhi-Hai Kou, Hong-Tao Lv, W. Zeng, Min-Li Bai, and Ji-Zu Lv, Comparison of different analytical models for heat and mass transfer characteristics of an evaporating meniscus in a micro-channel, Int. Commun. Heat Mass Transfer **63**, 49 (2015).

[45] H. K. Dhavaleswarapu, J. Y. Murthy, and S. V. Garimella, Numerical investigation of an evaporating meniscus in a channel, Int. J. Heat Mass Transf. **55**, 915 (2012).

[46] H. Wang, J. Y. Murthy, and S. V. Garimella, Transport from a volatile meniscus inside an open microtube, Int. J. Heat Mass Transf. **51**, 3007 (2008).

[47] R. Ranjan, J. Y. Murthy, and S. V. Garimella, A microscale model for thin-film evaporation in capillary wick structures, Int. J. Heat Mass Transf. **54**, 169 (2011).

[48] Z. Zheng, L. Zhou, X. Du, and Y. Yang, Numerical investigation on conjugate heat transfer of evaporating thin film in a sessile droplet, Int. J. Heat Mass Transf. **101**, 10 (2016).

[49] H. Yi, J. Tipton, K. D. Kihm, D. M. Pratt, A. D. Swanson, and S. Rawal, Effect of disjoining pressure (π) on multi-scale modeling for evaporative liquid metal (na) capillary, Int. J. Heat Mass Transf. **78**, 137 (2014).

[50] K. Bellur, An Assessment of the Validity of the Kinetic Model for Liquid-Vapor Phase Change by Examining Cryogenic Propellants, Master's thesis, Michigan Technological University, 2016.

[51] J. L. Plawsky, S. S. Panchamgam, S. J. Gokhale, P. C. Wayner, and S. DasGupta, A study of the oscillating corner meniscus in a vertical constrained vapor bubble system, Superlatt. Microstruct. **35**, 559 (2004).

[52] L. Zheng, J. L. Plawsky, P. C. Wayner, and S. DasGupta, Stability and oscillations in an evaporating corner meniscus, J. Heat Transf. **126**, 169 (2004).

[53] Thao T. T. Nguyen, J. Yu, J. L. Plawsky, P. C. Wayner, D. F. Chao, and R. J. Sicker, Spontaneously oscillating menisci: Maximizing evaporative heat transfer by inducing condensation, Int. J. Therm. Sci. **128**, 137 (2018).

[54] K. Bellur, E. F. Médici, M. Kulshreshtha, V. Konduru, D. Tyrewala, A. Tamilarasan, J. McQuillen, J. B. Leão, D. S. Hussey, D. L. Jacobson, J. Scherschligt, J. C. Hermanson, C. K. Choi, and J. S. Allen, A new experiment for investigating evaporation and condensation of cryogenic propellants, Cryogenics **74**, 131 (2016).

[55] C. H. Panzarella and M. Kassemi, On the validity of purely thermodynamic descriptions of two-phase cryogenic fluid storage, J. Fluid Mech. **484**, 41 (2003).

[56] C. Panzarella and M. Kassemi, One-dimensional model of evaporation and condensation in the presence of a noncondensable gas with applications to cryogenic fluid storage, Int. J. Heat Mass Transf. **52**, 3767 (2009).

[57] J. Hartwig and J. McQuillen, Analysis of screen channel LAD bubble point tests in liquid oxygen at elevated temperature, in *Proceedings of the 42nd AIAA Thermophysics Conference* (American Institute of Aeronautics and Astronautics, Honolulu, Hawaii, USA, 2011).

[58] Bellur, A new technique to determine accommodation coefficients of cryogenic propellants, Ph.D. thesis, Michigan Technological University, 2018.

[59] S. DasGupta, J. A. Schonberg, and P. C. Wayner, Investigation of an evaporating extended meniscus based on the augmented young–laplace equation, J. Heat Transf. **115**, 201 (1993).

[60] J. Israelachvili, *Intermolecular and Surface Forces* (Elsevier, Amsterdam, 2011).

[61] K. Bellur, Vinaykumar Konduru, E. F. Medici, D. S. Hussey, D. L. Jacobson, J. M. LaManna, J. S. Allen, and Chang Kyoung Choi, Visualization of the evaporation and condensation phenomena in cryogenic propellants, J. Flow Vis. Image Process. **23**, 137 (2016).

[62] K. Bellur, E. Medici, J. Allen, Chang Kyoung Choi, J. Hermanson, A. Tamilarasan, D. Hussey, D. Jacobson, J. B. Leao, and J. McQuillen, Neutron radiography of condensation and evaporation of hydrogen in a cryogenic condition, J. Heat Transf. **137**, 080901 (2015).

[63] K. Bellur, Vinaykumar Konduru, M. Kulshrestha, D. Tyrewala, E. Medici, J. S. Allen, Chang Kyoung Choi, D. S. Hussey, D. C. Jacobson, J. B. Leão, J. McQuillen, J. Hermanson, and A. Tamilarasan, Contact angle measurement of liquid hydrogen (LH2) in stainless steel and aluminum cells, J. Heat Transf. **138**, 020904 (2016).

[64] Vinaykumar Konduru, K. Bellur, E. F. Médici, J. S. Allen, Chang Kyoung Choi, D. S. Hussey, D. Jacobson, J. B. Leão, J. McQuillen, and J. C. Hermanson, Examining liquid hydrogen wettability using neutron imaging, J. Heat Transf. **138**, 080901 (2016).

[65] K. Bellur, D. Hussey, D. Jacobson, J. Lamana, E. Medici, J. Hermanson, Dr. Jeffrey S. Allen, and Chang Kyoung Choi, Neutron attenuation analysis of cryogenic propellants, J. Heat Transf. **140**, 030904 (2018).

[66] K. Bellur, E. F. Médici, J. C. Hermanson, C. K. Choi, and J. S. Allen, Determining solid-fluid interface temperature distribution during phase change of cryogenic propellants using transient thermal modeling, Cryogenics **91**, 103 (2018).